Conference paper: SEM Annual Conference & Exposition on Experimental & Applied Mechanics, June 13-15, 2011, Uncasville, CT.

Contact Mechanics of Impacting Slender Rods: Measurement and Analysis

Anthony Sanders[1], M.S., Ira Tibbitts[1], B.S., Deepika Kakarla[1], B.E., Stephanie Siskey[2], B.S., Jorge Ochoa[3], Ph.D., Kevin Ong[2], Ph.D., and Rebecca Brannon[1], Ph.D.
[1] University of Utah, Dept. of Mechanical Engineering, 2134 MEB, Salt Lake City, UT 84112
[2] Exponent, Inc., 3401 Market St., Suite 300, Philadelphia, PA, 19104
[3] Exponent, Inc., 15375 SE 30th Place, Suite 250, Bellevue, WA 98007

ABSTRACT

To validate models of contact mechanics in low speed structural impact, slender rods with curved tips were impacted in a drop tower, and measurements of the contact and vibration were compared to analytical and finite element (FE) models. The contact area was recorded using a thin-film transfer technique, and the contact duration was measured using electrical continuity. Strain gages recorded the vibratory strain in one rod, and a laser Doppler vibrometer measured velocity. The experiment was modeled analytically using a quasi-static Hertzian contact law and a system of delay differential equations. The FE model used axisymmetric elements, a penalty contact algorithm, and explicit time integration. A small submodel taken from the initial global model economically refined the analysis in the small contact region. Measured contact areas were within 6% of both models' predictions, peak speeds within 2%, cyclic strains within 12 microstrain (RMS value), and contact durations within 2 μs. The accuracy of the predictions for this simple test, as well as the versatility of the diagnostic tools, validates the theoretical and computational models, corroborates instrument calibration, and establishes confidence that the same methods may be used in an experimental and computational study of the impact mechanics of artificial hip joints.

1. Introduction

The problem of analyzing the impact of slender rods has previously been addressed in several classical works [1-3]. Recent approaches have included substructure analysis [4] and modal analysis combined with a Hertzian contact law [5,6]. FEA has been applied to problems of a single impacted rod [7,8] and two impacting rods [9], with results that have shown close fidelity to analytical models. Considering experimental approaches, contact duration between impacting metallic spheres and rods has been measured using electrical continuity [10,11]. Strain gages have been used to measure the strain waves in impacted rods [1,12-15]. Recently, laser vibrometry has been employed to measure the transient velocity on the surface of a rod impacted by a sphere [6,8,12,13]. Notably, the problem of a sphere striking the end of a long rod was formulated using a system of delay differential equations [12,13]. Viewing the effectiveness of this approach, one aim of the present work is to extend this recently demonstrated approach to the case of two impacting rods, and to add experimental validation of the predicted contact mechanics.

To date, neither the contact area nor contact stress generated by such impacts has been adequately analyzed and experimentally validated. It is difficult to experimentally record a small, transient elastic contact area; even so, practical methods have been described [16,17], including a recent one of our own design that uses inexpensive materials: grease and photocopier powder [18]. Accordingly, the second aim of the present work is to measure the contact area generated between impacting spherically tipped rods. The results will validate the analytical use of a Hertzian contact law to describe the force-displacement relation at the impact site.

Hertzian theory can provide comprehensive contact mechanics predictions [19,20], but its accuracy depends upon assumptions that may be ill-suited to some impact problems. FEA also provides a means of examining impact-induced contact stress; however, sufficient mesh refinement in the case of small contacts may require small elements that entail high computational cost. In the submodelling technique in FEA, the results of a coarsely meshed global model are applied as boundary conditions to a submodel of a small area of interest that requires a refined mesh. Submodelling has been applied in FEA where a contact area of interest was a small portion of a larger model [21,22].

Hence, two approaches, analytical and FEA, are suited to simulating the two-rod impact problem on both the macro and micro-scales. Likewise, experimental techniques may validate the simulations' results on both scales. Therefore, this work aims to demonstrate both simulation approaches and to compare their predictions with experimental outcomes, at both scales.

2. Methods and materials

2.1. Analytical model

The analysis begins with the schematic in Fig. 1. Rod 1 with speed s_1 travels axially and impacts stationary Rod 2. The rods are parallel, and the impact is centric. Dimensions d_i give the diameters, r_i the tip radii, and L_i the lengths. The rods' coordinates, x_1 and x_2, are measured inward from the radiused tip, and the rods are modeled as homogeneous, linear elastic, and isotropic; accordingly, the material properties are the densities ρ_i, elastic modulii E_i, and Poisson's ratios ν_i.

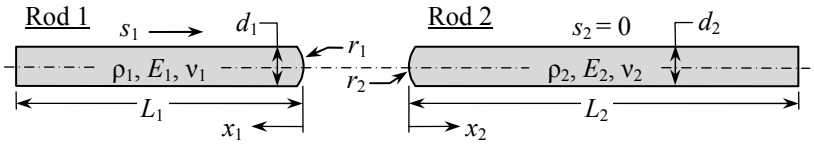

Fig. 1 Schematic for the axial, centric impact of two slender rods

The governing equation of each rod is approximately the 1D wave equation [1]. In Rod 2, the general solution is [23]:

$$u_2(x_2,t) = f_2(t - x_2/c_2) + g_2(t + x_2/c_2) \tag{1}$$

Here, u_2 is the displacement and $c_2=\sqrt{E_2/\rho_2}$ is the longitudinal wave speed. This solution represents two waves: right-traveling unknown function $f_2(\ )$ and left-traveling unknown function $g_2(\ )$ [1]. A similar equation applies to Rod 1, although a reversal of the left/right description applies since x_1 is *positive leftward*. The stress-free boundary condition at $x_2=L_2$ implies the strain-free condition $\partial u_2/\partial x_2=0$, which yields $g'_2(t+L_2/c_2)=f'_2(t-L_2/c_2)$, where $(')$ denotes differentiation with respect to the entire argument. This expression holds at an offset instant $t_o=t-L_2/c_2$, which yields:

$$g'_2(t) = f'_2(t - 2L_2/c_2) \tag{2}$$

At the impacted end ($x_2=0$), the strain is related to the stress via Hooke's law: $\partial u_2/\partial x_2=F(t)/E_2A_2$, where $F(t)$ is the contact force during impact and A_2 is the cross-sectional area. Applied to Eq. (1), this yields:

$$f'_2(t) = g'_2(t) - c_2F(t)/E_2A_2 \tag{3}$$

This assumes that the contact force is uniformly distributed across the impacted end, which is inaccurate in the vicinity of the contact, but is nevertheless appropriate to model the wave motion far from the point of contact based on St. Venant's principle. In the contact region, the contact force is related to the displacement by a Hertzian contact law [13]: $F(t)=-K[\delta(t)]^{3/2}$, where K is the Hertzian contact stiffness (addressed below), and $\delta(t)$ is the compression due to impact; the negative sign yields a compressive (negative) force and stress. The compression is the difference in rod displacements at the impacted ends: $\delta(t)=-u_1(0,t)-u_2(0,t)$, which treats the impacted ends' displacements as uniform over the cross-section of each rod.

In Rod 1, the strain rate at the free end ($x_1=L_1$) is zero: $\partial u_1/(\partial x_1\partial t)=[-f''_1(t-x_1/c_1)+g''_1(t+x_1/c_1)]/c_1=0$. This holds at an offset instant $t_o=t-L_1/c_1$, which yields:

$$g''_1(t) = f''_1(t - 2L_1/c_1) \tag{4}$$

Evaluating the strain rate at the impacted end ($x_1=0$) yields: $\partial u_1/(\partial x_1\partial t)=[-f''_1(t)+g''_1(t)]/c_1=F'(t)/E_1A_1$. Thus:

$$f''_1(t) = g''_1(t) + \tfrac{3}{2}(c_1K/E_1A_1)\sqrt{\delta(t)}\,\dot{\delta}(t) \tag{5}$$

The rate of compression in Eqn. (5) is derived from the compression relation, and it is given by:

$$\dot{\delta}(t) = -f'_1(t) - g'_1(t) - f'_2(t) - g'_2(t) \tag{6}$$

The governing system of differential equations of the system is thus given by Eqns. (2)-(6). The initial conditions are:

$$f_1(0)=0, \quad g_1(0)=0, \quad f_2(0)=0, \quad g_2(0)=0, \quad f'_1(0)=0, \quad g'_1(0)=-s_1 \tag{7}$$

The Hertzian stiffness is [24]:

$$K = \tfrac{4}{3}E^*\sqrt{R^*} \quad \text{with} \quad E^* = \left[(1-\nu_1^2)/E_1 + (1-\nu_2^2)/E_2\right]^{-1} \quad \text{and} \quad R^* = \sqrt{r_1r_2/(r_1+r_2)} \tag{8}$$

Various kinematic quantities may be determined using suitable derivatives of the wave equation for each rod. For instance, the speed and the strain at the midpoint of Rod 2 are:

$$\dot{u}_2(L_2/2,t) = f'_2(t - L_2/2c_2) + g'_2(t + L_2/2c_2) \qquad \varepsilon_2(L_2/2,t) = -\tfrac{1}{c_2}f'_2(t - L_2/2c_2) + \tfrac{1}{c_2}g'_2(t + L_2/2c_2) \tag{9}$$

The contact radius, a, and the peak contact pressure within that area, P, relate to the contact force as follows [24]:

$$a = \sqrt[3]{3FR^*/4E^*} \qquad P = 3F/2\pi a^2 \tag{10}$$

Solutions to the governing equations were computed using numerical integration using Simulink (Mathworks, Natick, MA). Integration was performed using the MATLAB function *ode45* [25]. The time delay was implemented using the *Transport Delay* function block. The model also computed kinematic quantities, e.g. Eq. (9).

2.2. Finite element model

The 3D global model comprised the geometries of both rods. The meshes were generated using HyperMesh (Altair, Troy, MI) and consisted of hexahedral elements with a longitudinal edge length of 1.0 mm and an average cross-section edge length of 0.25 mm (Fig. 2). The material model was linear elastic to represent the steel from which the rods were made (Sec. 2.3 below). Contact constraints were implemented using a penalty algorithm.

The submodel comprised the first 14 mm (measured from the impact tips) of both rods. This cutoff length was where the subsurface stresses diminished to near-zero magnitudes at the time of peak contact force in the global results. Three mesh refinements were used to examine convergence. The element aspect ratios were approximately 1:1:1, and the average edge length was successively halved in the refinement steps: from 0.25 (*Coarse*), to 0.125 (*Mid*), to 0.0625 mm (*Fine*) (first 2 models, Fig. 2b and 2c). The Fine submodel was additionally simplified as a half-symmetry model. The physical configuration of the rods is detailed in Table 1. The impact speed, 2.197 m/s, was a value recorded during one of the experimental trials. The finite element solver Abaqus/Explicit (Abaqus v. 6.8, Simulia, Providence, RI) was used to perform the global and submodel analyses. The 8-node linear hexahedral element type with uniform strain and hourglass control (C3D8R; reduced integration element) was implemented for both rods.

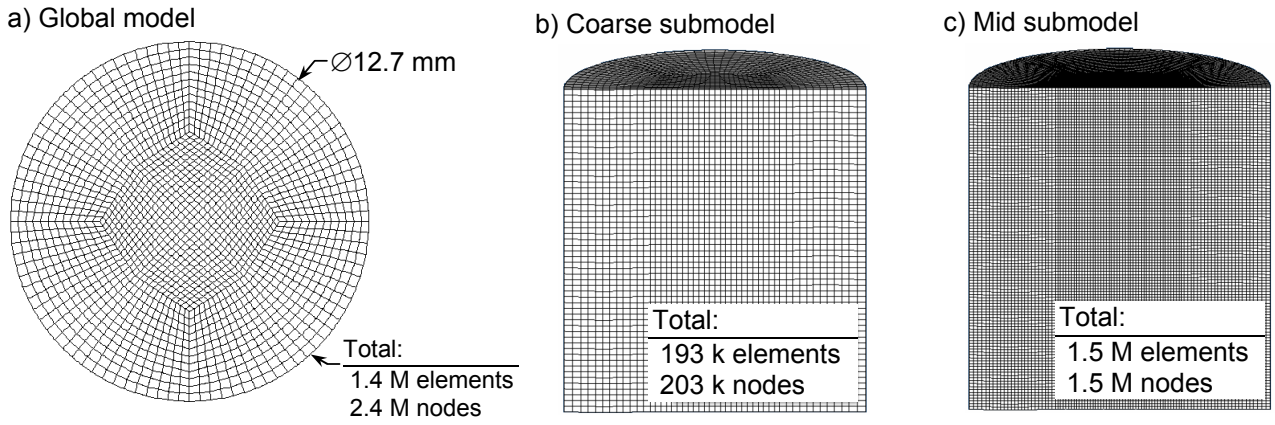

Fig. 2 Cross sections of the FE meshes in each rod: a) Global 3D model, b) Coarse submodel, c) Mid submodel. Submodels were also cylindrical, but shown as halved to display element density

Table 1 Physical configuration details of the finite element model

Rod 1 length	Rod 1 r_1	Rod 2 length	Rod 2 tip	Diameter	Density	Young's modulus	Poisson's ratio	Impact speed
250.09 mm	35 mm	700.99 mm	flat	12.70 mm	7.803 g/cc	204.3 GPa	0.30	2.197 m/s

2.3. Experimental techniques

Both rods were made from a single lot of precision ground A2 steel drill rod. The spherical tip of Rod 1 was finished using a concave 35 mm radius cast iron lap charged with diamond particles. The flat tip of Rod 2 was lapped against a granite surface plate using fine grit silicon carbide sandpaper. (Due to the flat tip, $r_2 \to \infty$ in Eq. (8), so $R^*=r_1$.) There were three specimens of Rod 1 to allow repeat trials, and one of Rod 2. The rods were hardened and tempered to R_c 60. The density was determined from the volume and the mass of one specimen; length was measured using a height gauge, diameter using a micrometer, and mass using an analytic balance. The isentropic elastic properties were measured using the impulse excitation method, ASTM

E 1876, using a Grindosonic MK5 instrument (Lemmens, Lueven, BLG). Further, the experiments were designed to maintain contact stresses within the material's linear elastic region; the criterion $P < 1.1S_y$, where S_y is the uniaxial yield stress [26] was upheld by the experimental design.

The impact experiments were performed in a drop-tower test machine (Dynatup 8250, Instron, Massachusetts, USA) (schematic Fig. 3). The machine provides a motorized latch block that suspends a sled. Upon computer command, the sled may be released from the latch block into free fall guided by twin columns. To the sled was mounted a tubular fixture that suspends Rod 1; the rod was spaced off the tube's interior surface by 2 oiled o-rings. The rod's weight was suspended by a thin ring of tape whose diameter was slightly greater than the tube's ID; otherwise, Rod 1 was distally unconstrained. Rod 2 was suspended in a tubular fixture attached to the test machine base; this fixture also spaced its rod from the interior surface via oiled o-rings. Both fixtures provided approximately 6 cm of clearance behind the rods' distal ends, spaces into which the rods could slide freely after impact. Rod 2 was partly supported on its distal end by a plastic plug lightly press-fit into the tube; the plug could fall freely into the fixture's clearance space when Rod 2 was impacted. The position of the lower fixture was adjustable to permit manual alignment of the rods to achieve parallel, centric impact. The velocity of the sled was measured using an infrared sensor fixed to the drop tower that sensed passage of a flag mounted to the sled. The sensor was positioned to detect velocity at the impact position, and it was assumed that Rod 1's velocity was equal to the sled's velocity. In repeat trials, the impact speed varied slightly (±0.02 m/s) because the drop height was not precisely repeatable.

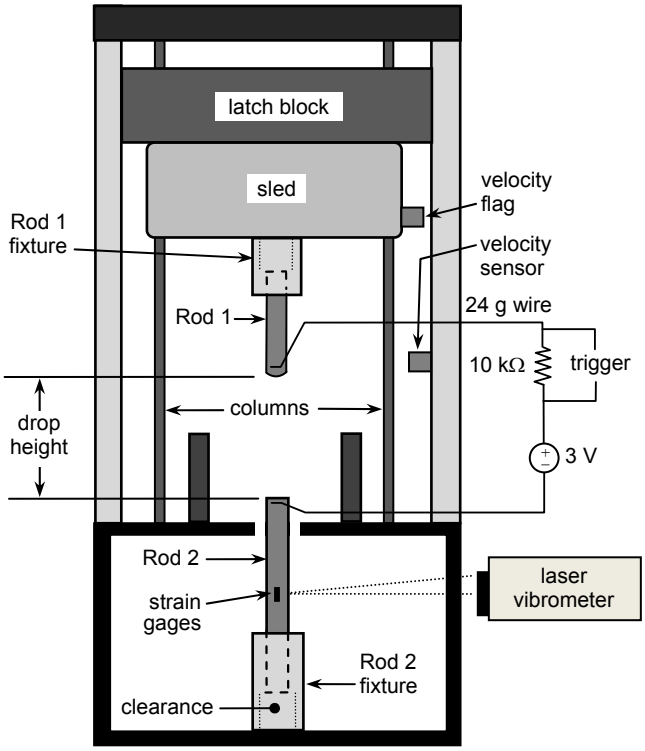

Fig. 3 Schematic of drop tower impact test machine, with both rods, their fixtures, and trigger circuit; data acquisition and strain gage circuit not illustrated

Both rods were wired into an electrical circuit by taping to each a 24 gauge, multi-filament wire. The circuit charged Rod 1 to 3 V relative to Rod 2 using an electrical power supply. Continuity between the rods during impact created a voltage across a 10 kΩ resistor, and the voltage was used to trigger data acquisition and to measure the duration of impact.

The velocity of Rod 2 was measured at its midpoint using a 3D laser Doppler vibrometer (CLV-3D, Polytec, Germany). The vibrometer provided 3 separate, orthogonal velocity components, but only the component parallel to the rod's surface was recorded. Strain was measured at Rod 2's midpoint using two 1000Ω foil strain gages (WC-06-125AC-W/C, MicroMeasurements, Raleigh, NC, USA) oriented to measure axial strain and wired into opposing arms of a Wheatstone bridge. This circuit design doubled the bridge sensitivity compared to a circuit with only one active gage. The bridge was powered and its output signal was amplified using a high bandwidth signal conditioner (2310B, MicroMeasurements). Use of 1000Ω gages permitted maximal excitation of the bridge (15 V); so, the amplifier gain was set relatively low (~110), which

enhanced the amplifier's frequency response quality (-3 dB bandwidth of 230 kHz). The bridge and amplifier were calibrated using a shunt calibration procedure [27]. The three measurement signals were recorded at 443 kHz using a 16 bit analog-to-digital (A/D) converter (USB1604HS, Measurement Computing, Norton, MA, USA) controlled by a laptop computer. To enhance A/D accuracy, the input range of each A/D channel was programmed to limits just greater than the maximal signal value; thus, the ranges for velocity and strain were ±10 V, and ±0.5 V, respectively.

A record of the contact between the rods was made using a "fingerprinting" technique. The tip of Rod 2 was given a thin coat of bearing grease. The tip was wiped repeatedly (16 times), each time using a clean piece of paper towel, to leave a scant grease film. The tip of Rod 1 was cleaned with warm, soapy water and thoroughly rinsed and dried. During contact, a thin spot of grease transferred from Rod 2 onto Rod 1. After the test, the entire tip of Rod 1 was sprinkled with black photocopier toner powder. The powder was blown off with an aerosol duster can. A monoparticle layer of powder (the "fingerprint") remained adhered to the thin transfer layer of grease. This patch was then microscopically measured and photographed using an optical coordinate measuring machine ('CMM', Nexiv VMR 3020, Nikon, JPN). The CMM detected edge points by analyzing contrast levels in the digital image of the contact patch; 64 points were found at uniform spacing around the patch's perimeter, and these were used to compute the radius and circularity of a best-fit circle.

3. Results

The recorded velocity and strain at the midpoint of Rod 2 are graphed with the analytical and FEA predictions in Fig. 4. Also, the contact force from both models is superimposed with the contact trigger voltage. Non-scaled transducer voltage data from the experimental velocity and strain records (Fig. 4d) demonstrate the sufficiency of the A/D sampling rate.

Fig. 5 gives photos of the recorded contact patch on the tip of Rod 1, along with a contour plot of the contact pressure from the global FE model. The images show the circular contact patch that has been revealed by black toner powder adhering to the thin layer of grease transferred from the tip of Rod 2.

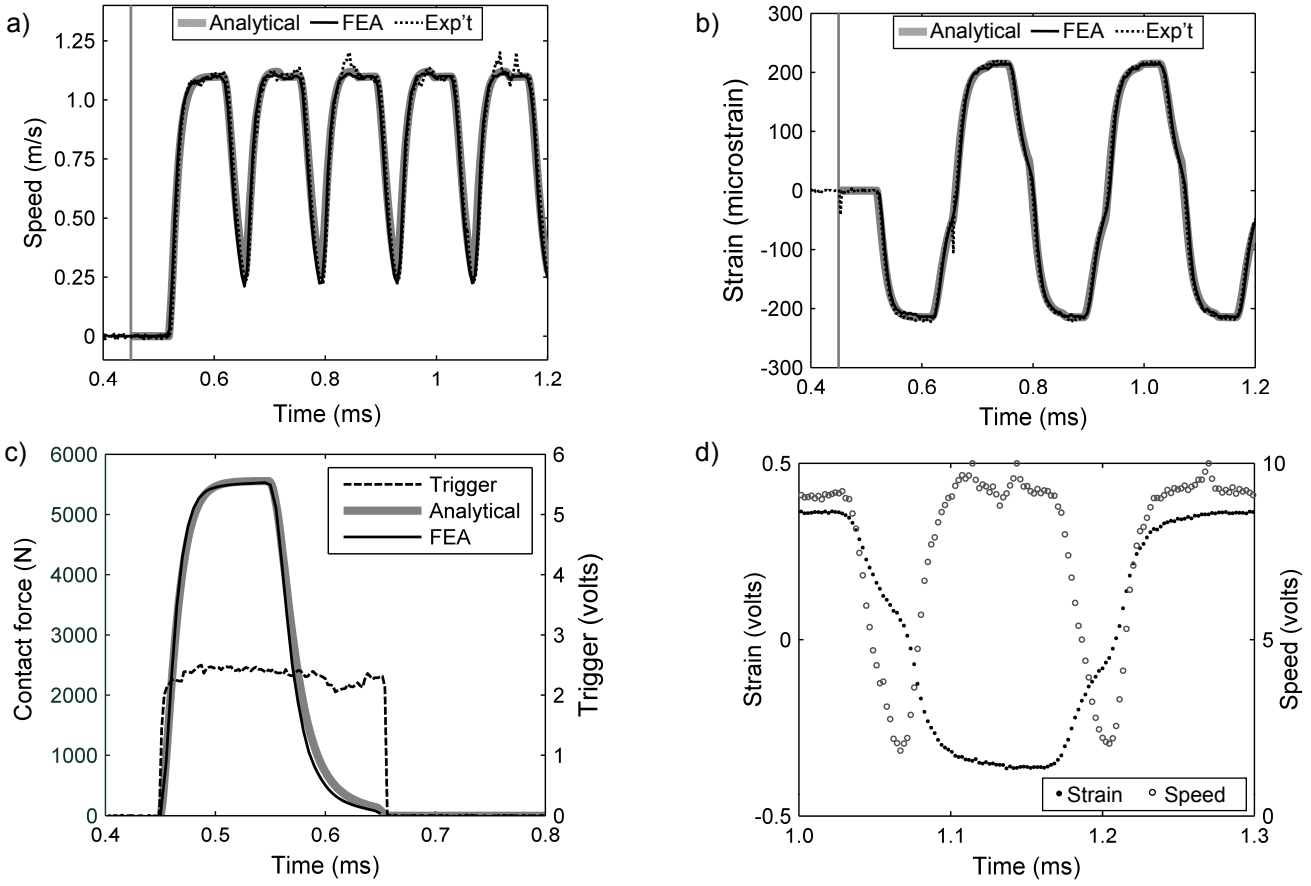

Fig. 4 Global model results: a) Speed and b) Strain at midpoint of Rod 2, vertical line at trigger instant; c) Contact force and trigger signal; d) Samples of non-scaled voltage data points for speed and strain

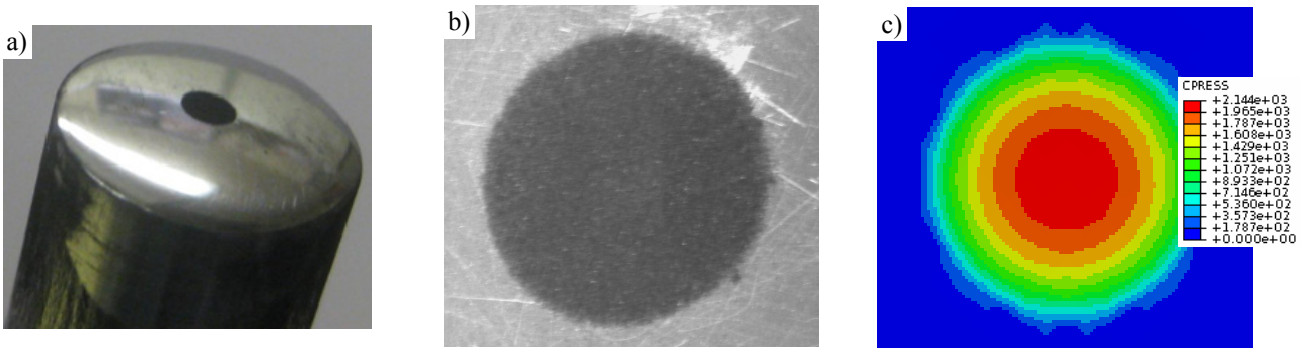

Fig. 5 a) and b): Images of a typical contact patch, ~∅2.2 mm, recorded by the "fingerprinting" technique: a) from handheld camera, b) from optical CMM, original magnification 37×. c) Plot of contact pressure from global FEA, same scale as b)

Table 2 compares experimental to analytical model results in 2 trials of each Rod 1 specimen. The circularity (as defined by ASME Y14.5M) of the measured contact patch was 7-8% of the radius in Specimens 1 and 3, but 11-12% in Specimen 2, perhaps indicating that Specimen 2 had more form error in its spherical tip. The predicted contact radius was at most 5% less than measured. The peak speed at the midpoint of Rod 2, consisting of values ≥1.0 mm/s, was averaged over the first five plateaus in the record; the maximum difference was 2.2%. The root-mean-square (RMS) of the difference in strain was computed over the first five periods; the maximum RMS difference was 11.6 microstrain. The FEA model used the impact speed of Rod 1, Spec. 1, Trial 3. Table 3 shows the contact force and contact area for the global model and the three meshes in the submodel. The contact radius (from $r=\sqrt{(area/\pi)}$) of the Fine submodel was 1.14 mm (+2.8% vs. expt.). Fig. 6 compares the analytical and FEA results of the radial stress component, σ_r, as a function of radial coordinate. The stresses were extracted from the element integration points closest to the surface, and the analytical results were computed at identical points using formulas in [26].

Table 2 Results from two trials of each Rod 1 specimen. 'Analytical' gives value and difference from experiment. 'RMS Δ' is the root-mean-square difference

			Contact radius (mm)			Rod 2 midpoint		
Rod 1 specimen	Trial #	Impact speed (m/s)	Experimental		Analytical	Avg. peak speed (mm/s)		RMS Δ strain (microstrain)
			Circularity	radius	radius	Exp't	Analytical	
1	1	2.208	0.098	1.129	1.093 (-3.2%)	-	-	-
	3	2.197	0.091	1.109	1.090 (-1.7%)	1.114	1.105 (-0.8%)	6.0
2	4	2.178	0.140	1.143	1.087 (-4.9%)	1.105	1.095 (-0.9%)	11.6
	5	1.848	0.117	1.059	1.029 (-2.8%)	0.921	0.930 (+0.9%)	3.4
3	2	2.166	0.090	1.120	1.085 (-3.2%)	1.114	1.089 (-2.2%)	7.4
	3	2.128	0.083	1.115	1.079 (-3.2%)	1.078	1.070 (-0.7%)	5.0
Average Δ (absolute value)					3.2%	-	1.1%	6.7

Table 3 Contact force and area from the global model and three refinement levels of the submodel

Model	Contact force (N)	Contact area (mm^2)
Global	5,549	4.61
Submodel-Coarse	5,219	4.80
Submodel-Medium	5,368	4.44
Submodel-Fine	5,492	4.10
Analytical / Experimental	5,543	3.73 / 3.86
Δ, Fine vs. Analytical / Exp't	-0.92%	9.9% / 6.2%

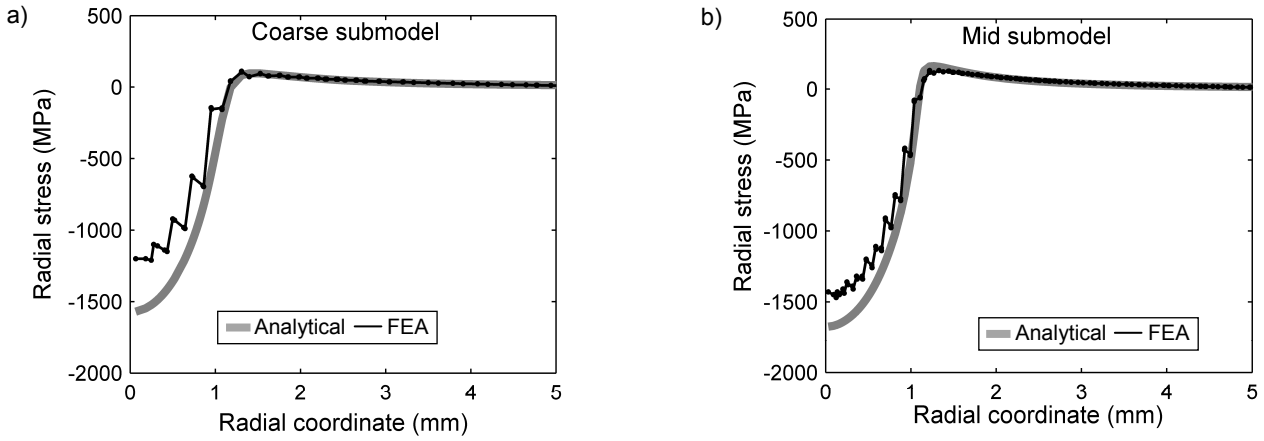

Fig. 6 Comparison of analytical and FEA subsurface radial stress result, σ_r, from element integration points

4. Discussion and Conclusions

Both of the analysis models aimed to give high fidelity predictions of the global structural response. The analytical model predicted the peak Rod 2 midpoint speed within 0.7-2.2% error. Likewise, the model's strain prediction had an RMS error (over 5 periods of the vibration) of 3.4-11.6 microstrain (Table 2). Though not tabulated, the error of the model's contact duration prediction was only 1-2 μs, which is approximately the value of the sampling period. The FE model yielded similar fidelity, with the plots of its results nearly overlying those from the analytical model in Fig. 4. Similarly accurate predictions of global structural response, from both analytical and FE models, have been reported for the case of a ball striking a long rod [8,12,13], though without direct measurement of the contact duration and contact area.

The chief aim of submodelling was to provide a refined FEA focused on the contact mechanics. The peak contact radius during impact was ~1 mm, so the 0.25×0.25×1.0 mm elements in the global model were expected to yield relatively coarse resolution of the contact stress and area, since contact stress fields are quite localized [26]. The use of three submodel mesh refinements with successively halved element lengths has been previously recommended [21]. In the first submodel, the contact force differed by -330 N from the global model; the change occurred because mesh refinement reduced the stiffness of the contact surfaces while nodal displacements from the global model were applied to the submodel boundary. This effect diminished with subsequent mesh refinements, finally yielding a contact force <1% different from the analytical model and contact area 6.2% different from the experimental measurement. Ongoing work is expected to improve the FEA results in contact area and in the convergence of particular stress values; the existence of some non-convergent stress values in the half-symmetry Fine submodel has revealed that some nodes were minutely displaced from the symmetry plane.

The impact of slender rods provides a means for examining fundamental characteristics of the transient dynamics of impacting bodies. These include material property effects, speeds of wave propagation, and contact mechanics. A basic understanding of these dynamic phenomena, as they occur in the approximately 1D domain of slender rods, is an important pre-requisite to advanced impact analysis and testing involving more complicated structures. In contrast with the case of a ball–rod impact, the case of two impacting rods requires consideration of vibrations in both bodies, which may be more representative of complicated impact scenarios.

In our laboratory, this study has served as a means to verify and validate analysis and laboratory techniques for studying the transient dynamics of artificial hip joints. An artificial hip may experience small (e.g. 2 mm) separations of the ball from the socket [28], followed by rapid relocation that causes high and damaging contact stresses [29]. The hip study's objective is to identify peak contact force and stress during the rapid relocation phase, and these quantities cannot be directly measured. Therefore, they are being computed using an FE model of a corresponding dynamically actuated structure in an in-vitro relocation simulation. To validate the FE model, the structure's response to the inputs is measured using laser vibrometry and strain gages with high-bandwidth amplification, as used for the two-rod impact study. Thus, the present work has validated measurement and analysis techniques in a rudimentary test case, so that they may be applied confidently to a challenging biomedical problem. The engineering approach to impact problems in other fields may benefit similarly by preparatory testing and analysis of the low speed impact of slender rods.

Acknowledgements
The authors are grateful to Jeff Kessler for laboratory assistance, in particular with the drop tower impact test machine.

References
[1] Timoshenko, S.P., and Goodier, J.N., *Theory of Elasticity*, McGraw Hill, New York, 1970.
[2] Thomson, W.T., *Laplace Transformation*, Prentice Hall, Englewood Cliffs, 1960.
[3] Goldsmith, W., *Impact: The Theory and Physical Behaviour of Colliding Solids*, Edward Arnold, Ltd., London, 1960.
[4] Guo, A., and Batzer, S., "Substructure Analysis of a Flexible System Contact-Impact Event," Journal of Vibration and Acoustics, 126(1), 126-131, 2004.
[5] Marghitu, D.B., and Boghiu, D., "Spatial Impact of a Flexible Link Using a Nonlinear Contact Force," Atlanta, GA, USA, 90, 103-110, 1996
[6] Schiehlen, W., and Seifried, R., "Three Approaches for Elastodynamic Contact in Multibody Systems," Multibody System Dynamics, 12(1), 1-16, 2004.
[7] Trowbridge, D.A., et al., "Low Velocity Impact Analysis with Nastran," Computers and Structures, 40(4), 977-984, 1991.
[8] Seifried, R., and Hu, B., "Numerical and Experimental Investigation of Radial Impacts on a Half-Circular Plate," Multibody System Dynamics, 9(3), 265-81, 2003.
[9] Wei, H., and Yida, Z., "Finite Element Analysis on Collision between Two Moving Elastic Bodies at Low Velocities," Computers and Structures, 57(3), 379-82, 1995.
[10] Stoianovici, D., and Hurmuzlu, Y., "A Critical Study of the Applicability of Rigid-Body Collision Theory," Transactions of the ASME. Journal of Applied Mechanics, 63(2), 307-16, 1996.
[11] Bokor, A., and Leventhall, H.G., "The Measurement of Initial Impact Velocity and Contact Time," Journal of Physics D: Applied Physics, 4(1), 160-163, 1971.
[12] Hu, B., and Eberhard, P., "Simulation of Longitudinal Impact Waves Using Time Delayed Systems," Journal of Dynamic Systems, Measurement and Control, Transactions of the ASME, 126(3), 644-649, 2004.
[13] Hu, B., et al., "Comparison of Analytical and Experimental Results for Longitudinal Impacts on Elastic Rods," Journal of Vibration and Control, 9(1-2), 157-74, 2003.
[14] Sundin, K.G., and Ahrstrom, B.O., "Method for Investigation of Frictional Properties at Impact Loading," Journal of Sound and Vibration, 222(4), 669-77, 1999.
[15] Ueda, K., and Umeda, A., "Dynamic Response of Strain Gages up to 300 Khz," Experimental Mechanics, 38(2), 93-98, 1998.
[16] Hertz, H., "On the Contact of Rigid Elastic Solids and on Hardness", in *Miscellaneous Papers by H. Hertz*, MacMillan, London, 1882.
[17] Diaconescu, E.N., et al., "A New Experimental Technique to Measure Contact Pressure," Ponte Vedra Beach, FL, USA, 121-128, 2003
[18] Sanders, A.P., and Brannon, R.M., "Determining a Surrogate Contact Pair in a Hertzian Contact Problem," Journal of Tribology, accepted for publication
[19] Fabrikant, V.I., "A New Symbolism for Solving the Hertz Contact Problem," Quarterly Journal of Mechanics and Applied Mathematics, 58, 367-81, 2005.
[20] Sackfield, A., and Hills, D.A., "Some Useful Results in the Classical Hertz Contact Problem," Journal of Strain Analysis for Engineering Design, 18(2), 101-105, 1983.
[21] Cormier, N.G., et al., "Aggressive Submodelling of Stress Concentrations," International Journal for Numerical Methods in Engineering, 46, 889-909, 1999.
[22] Rajasekaran, R., and Nowell, D., "On the Finite Element Analysis of Contacting Bodies Using Submodelling," Journal of Strain Analysis for Engineering Design, 40, 95-106, 2005.
[23] Drumheller, D.S., *Introduction to Wave Propagation in Nonlinear Fluids and Solids*, Cambridge University Press, Cambridge, 1998.
[24] Johnson, K.L., *Contact Mechanics*, Cambridge University Press, Cambridge, 1985.
[25] Shampine, L.F., and Reichelt, M.W., "The Matlab Ode Suite," SIAM Journal on Scientific Computing, 18(1), 1, 1997.
[26] Fischer-Cripps, A.C., *Introduction to Contact Mechanics*, *Mechanical Engineering Series*, Springer-Verlag, New York, 2000.
[27] "Tech Note Tn-514: Shunt Calibration of Strain Gage Instrumentation," Vishay Micro-Measurements, 2007.
[28] Lombardi, A.V., et al., "An in Vivo Determination of Total Hip Arthroplasty Pistoning During Activity," J Arthroplasty, 15(6), 702-709, 2000.
[29] Mak, M.M., et al., "Effect of Microseparation on Contact Mechanics in Ceramic-on-Ceramic Hip Joint Replacements," Proc Inst Mech Eng [H], 216(6), 403-408, 2002.